1

ON THE CONSISTENCY OF HNO_3 AND NO_2 IN THE ALEUTIAN HIGH

REGION FROM THE NIMBUS 7 LIMS VERSION 6 DATASET

4

Ellis Remsberg[1], Murali Natarajan[1], and V. Lynn Harvey[2]

6

7

[1]Science Directorate, NASA Langley Research Center

21 Langley Blvd, Mail Stop 401B

Hampton, Virginia 23681, USA

11

[2]Laboratory for Atmospheric and Space Physics

Atmospheric and Oceanic Sciences

University of Colorado, UCB 311

Boulder, Colorado, 80309, USA

16

Correspondence to: Ellis Remsberg (ellis.e.remsberg@nasa.gov)

18

19   **Abstract.** This study uses photochemical calculations along kinematic trajectories in conjunction with

20   Limb Infrared Monitor of the Stratosphere (LIMS) observations to examine the changes in HNO_3 and

21   NO_2 near 30 hPa in the region of the Aleutian High (AH) during the minor warming event of January

22   1979. An earlier analysis of Version 5 (V5) LIMS data indicated increases in HNO_3 without a

23   corresponding decrease in NO_2 in that region and a quasi-wave 2 signature in the zonal distribution of

24   HNO_3, unlike the wave 1 signal in ozone and other tracers. Version 6 (V6) LIMS also shows an increase

25   of HNO_3 in that region, but NO_2 is smaller than from V5. The focus here is to convey that V6 HNO_3 and

26   NO_2 are of good quality, as shown by a re-examination of their mutual changes in the AH region.

27   Photochemical model calculations initialized with LIMS V6 data show increases of about 2 ppbv in

28   HNO_3 over 10 days along trajectories terminating in the AH region on 28 January. Those increases are

29   mainly a result of the nighttime heterogeneous conversion of N_2O_5 on background stratospheric sulfuric

30   acid aerosols. Changes in the composition of the air parcels depend on the extent of exposure to sunlight

31   and, hence, on the dynamically controlled history of the trajectories. Trajectories that begin in low

32   latitudes and traverse to across the Pole in a short time lead to the low HNO_3 in the region separating the

33   anticyclone from the polar vortex, both of which contain higher HNO_3. These findings help to explain the

34   observed seasonal evolution and areal extent of both species. V6 HNO_3 and NO_2 are suitable, within their

35   errors, for the validation of stratospheric chemistry/climate models.

36

37

1 Introduction and Objectives

The Limb Infrared Monitor of the Stratosphere (LIMS) experiment operated on Nimbus 7 from 25 October 1978 through 28 May 1979. LIMS measurements were originally processed and archived to a Version 5 (V5) data set (see Gille and Russell, 1984, and references therein). Since then, the observed LIMS radiance profiles have been re-processed with improved, Version 6 (V6) algorithms to provide profiles of temperature, chemical species, and geopotential height, as a function of pressure-altitude from 65° S to 84° N latitude (Remsberg et al., 2004). There are improvements from the registration of the LIMS radiance profiles and from updated spectroscopic line parameters for retrievals of the V6 species profiles. Several studies already show that the V6 ozone is of better quality for scientific analysis (Natarajan et al., 2002; Stolarski et al., 2013; Remsberg et al., 2013; Shepherd et al., 2014). The two nitrogen species, nitric acid (HNO_3) and nitrogen dioxide (NO_2), are also of better quality, particularly NO_2 (Remsberg et al., 2010; Remsberg et al., 1994). Holt et al. (2012) quantified the exchange of V6 NO_2 from the mesosphere to the middle stratosphere within the polar vortex. Remsberg and Harvey (2016) also found good relationships on the 550 K potential temperature surface (near 30 hPa) for the highest values of V6 HNO_3, lowest values of ozone, and highest values of potential vorticity (PV) within the Arctic winter vortex. While there are residual effects from polar stratospheric clouds (PSCs) in the ozone and water vapor (H_2O), those effects are small in the HNO_3 and NO_2 profiles and occur only at temperatures < 194 K and from about 1-20 January. The V6 data set is part of the SPARC Data Initiative for chemistry-climate model comparison studies (Tegtmeier, et al., 2013; SPARC, 2017).

Northern hemisphere (NH) polar winter of 1978-1979 was dynamically active in the middle stratosphere, as determined from daily surface plots of geopotential height (GPH), potential vorticity (PV), and ozone on the 850 K potential temperature surface (near 10 hPa) (McIntyre and Palmer, 1983; Leovy et al., 1985; Butchart and Remsberg, 1986). A major, zonal wave 1 forcing brought about a rapid exchange of air

3

62 between polar and middle latitudes from mid to late January. Rood et al. (1993) (hereafter referred to as

63 R93) analyzed the LIMS V5 data in the Aleutian High (or AH) region for 14-27 January. They reported

64 that the tracer-like species HNO_3 on the 30-hPa surface increased slowly during that time in the region of

65 the relatively warm anticyclone. The absence in their analysis of a corresponding decrease in NO_2

66 accompanying the increase in HNO_3 led to concerns of an inconsistency in the LIMS data. The present

67 study reconsiders that anomaly but using the V6 dataset and a trajectory model that includes the chemistry

68 of reactive nitrogen (NO_y), or the sum of NO, NO_2, $2N_2O_5$, NO_3, HNO_3, HO_2NO_2, and $ClONO_2$.

69

70 In their analysis of the V5 data, R93 also noted finding high values of HNO_3 in both the polar vortex and

71 the AH, and lower values around the periphery of both circulation systems resulting in a quasi-wave 2

72 signature in the HNO_3 distribution. They suggested that, since dynamically controlled species like ozone

73 showed a clear wave-1 signature similar to GPH and PV, the HNO_3 levels outside the polar vortex may

74 have influences from a combination of chemistry and dynamics in order to account for its quasi-wave 2

75 variation. They explored the possible role of heterogeneous chemistry on background sulfate aerosols in

76 converting NO_x to HNO_3 and concluded based on a 2-D model study that those species changes from V5

77 are large in winter but not correct phenomenologically. Separate studies have shown that heterogeneous

78 reactions involving sulfate aerosols do perturb the stratospheric photochemistry and HNO_3 levels (Austin

79 et al., 1986; Rodriguez et al., 1991). With the availability of the improved V6 dataset, we revisit the

80 question of inconsistency for the LIMS HNO_3 and NO_2 observations in the AH region. We focus our

81 attention on the same period, namely $14 - 27$ January, when there was a minor stratospheric warming.

82

83 Section 2 describes briefly the improvements implemented in the retrievals of the V6 profiles. We also

84 note that the residual effects from unscreened PSCs in the polar vortex are small for HNO_3 relative to

85 those in ozone. Section 3 contains polar plots of ozone, HNO_3, NO_2, and GPH for 17 and 27 January

86   1979 and describes their changes, as the AH develops and the center of the vortex moves off the Pole.

87   Section 4 shows the changes in V6 HNO_3 and NO_2 at the center of the AH from 14 to 27 January.

88   Section 5 describes an ensemble of trajectory calculations, including heterogeneous chemistry, for air

89   parcels converging in the region of the AH on 27 January. Those calculations partition NO_y into the

90   observed HNO_3 and NO_2, plus the unobserved variations of nitric oxide (NO) and nitrogen pentoxide

91   (N_2O_5). The calculated daily species values compare reasonably well with closest observed LIMS values,

92   as shown from the results in Section 6. We then show in Section 7 time series of variations of PV and of

93   V6 HNO_3, H_2O, and NO_2 on the 550 K potential temperature surface across most of the northern

94   hemisphere for the entire 7¼ months of LIMS data. In this way, the variations for January are set in the

95   context of the longer-term, seasonal changes for those species. Section 8 is a summary of the findings.

96

97   **2 Improvements of the LIMS V6 species**

98   The LIMS instrument obtained profiles of atmospheric limb radiance in six channels, a wide (W) and a

99   narrow (N) band channel for CO_2 (CO_2W and CO_2N) and one each for ozone, H_2O, HNO_3, and NO_2

100   (Gille and Russell, 1984). Retrieved V6 profiles occur at a spacing of every 1.4° of latitude (~155 km)

101   along the orbit, although their horizontal, tangent-path resolution remains no better than about 320 km.

102   Bandpass filters (in cm^{-1}) for the LIMS instrument are CO_2W (579-755), CO_2N (637-673), ozone (926-

103   1141), H_2O (1370-1560), HNO_3 (844-917), and NO_2 (1560-1630) in terms of their 5 % relative response

104   points. Both the H_2O and NO_2 channels have an instantaneous field-of-view (IFOV) vertical width at the

105   horizon of 3.6 km, while the other four channels have half that width or 1.8 km.

106

107   Retrievals of the V6 temperature and associated species profiles were obtained by using all successive,

108   up/down scan profile pairs along their observed, orbital tangent-path locations and at 18 levels per decade

109   of pressure-altitude, p(z), or spaced about every 0.88 km. The effective vertical resolution is the same

110 (~3.7 km) for the retrieved V6 temperature and for each of the species profiles (Remsberg et al., 2004),

111 such that one can evaluate better the combined changes of HNO_3 and NO_2 at a given pressure-level.

112 Further, the spectral line parameters used for the retrieval of the NO_2 were updated for the production of

113 V6, leading to values of nighttime NO_2 that are up to 20 % smaller than those of V5 in the upper and

114 middle stratosphere (e.g., Remsberg et al., 1994). An important addition to the V6 data set is the co-

115 located GPH for each of the retrieved profiles.

116

117 LIMS-retrieved ozone has a non-linear sensitivity to temperature and/or radiance biases and to the effects

118 of PSCs; retrieved H_2O mixing ratio is even more sensitive (Remsberg et al., 2007; 2009). On the other

119 hand, effects from PSCs are much less noticeable in HNO_3 and NO_2. As an example, Figure 1 shows the

120 relative effects for ozone and HNO_3 of the residual contamination or the unscreened effects of emission

121 from PSCs, plus the associated temperature and GPH on the 31.6-hPa surface for 11 January. Grid-point

122 data for the surface plots of Fig. 1 are from the V6 Level 3 sequential estimation (SE) algorithm product

123 (Remsberg and Lingenfelser, 2010). The ozone panel of Fig. 1 shows values in the cold vortex region

124 that are of the order of 6 ppmv and not in keeping with the much lower surrounding values of 3 ppmv.

125 White plus signs indicate where there was a screening of profile segments perturbed by emissions from

126 PSCs in ozone, and the red dot indicates the presence of a PSC based on data from the Stratospheric

127 Aerosol Monitor (SAM II) experiment for comparison purposes. While there can be descent of ozone in

128 the vortex from higher altitudes, the excess ozone in the vortex region of Fig. 1 is due to the remaining,

129 unscreened effects of the PSCs. Note also that the PSC features occur only where the environmental

130 temperature is less than about 194 K. Thus, effects of PSCs are minimal for most of the Arctic lower

131 stratosphere, and they are not present at all in the warmer AH region.

132

133   The lower right panel of Fig. 1 shows that observed HNO_3 is highest in the vortex, and particularly in the

134   presence of PSCs. As HNO_3 adsorbs onto PSCs, a decrease of gas-phase HNO_3 is also expected in the

135   presence of and directly downwind of large PSCs (von Koenig et al., 2002; Lambert et al., 2012). Yet,

136   those high LIMS values are nearly unaffected by PSCs because the relationship between the LIMS HNO_3

137   channel radiance and its retrieved mixing ratio is essentially linear. In fact, simulation studies indicate

138   that a temperature bias error of 1 K has only a small, 3 % effect in the V6 HNO_3 mixing ratios from 10 to

139   50 hPa (Remsberg et al., 2010, their Table 1). Retrieved NO_2 also varies in a nearly linear way. Yet as

140   with ozone, there are no perturbing effects from PSCs for H_2O, HNO_3, or NO_2 in the AH region that is the

141   focus of the remainder of this study.

142

143   **3 LIMS V6 GPH, O_3, HNO_3, and NO_2 during January 1979**

144   R93 (and references therein) analyzed and presented results of GPH, ozone, and HNO_3 at 30 hPa from the

145   V5 data set for 14, 17, 23, and 27 January. They noted that ozone behaves as a tracer in terms of its

146   relation to changes in GPH and according to its associated transport fields. On the other hand, they found

147   that the HNO_3 distributions did not evolve in the same way, but developed a quasi-wave 2 rather than

148   wave 1 character over a deep layer of the middle stratosphere (50 to 5 hPa). They also did not find clear

149   anti-correlations between the distributions of V5 HNO_3 and NO_2 in the more isolated AH region, at least

150   to the extent that the sum of those two gases do not change appreciably. We consider their variations

151   again using the V6 data.

152

153   Initially, Rood et al. (1987) expressed some doubt about the accuracy of the Arctic GPH fields at 30 hPa

154   from the operational meteorological analyses for January 1979. Figs. 2b and 3b are polar plots of the

155   zonal GPH anomalies for the equivalent level of 31.6 hPa and for two of the four days above, 17 and 27

156   January. Those GPH anomalies exhibit structures that are very similar to those found by R93 (their Figs.

157   1b and 1d). Large-scale flow is along isolines of the GPH anomalies or around the respective high and

158   low centers. The AH strengthened significantly but remained at about the same location from 17-27

159   January.

160

161   Anomalies for the LIMS species in Figs. 2 and 3 are a result of subtracting the V6 zonal mean coefficient

162   (or mixing ratio) from the observed values at each latitude/longitude grid point. However, the so-called

163   "zonal anomalies" for ascending (local 1 pm) and descending (local 11 pm) NO_2 represent the result of

164   subtracting the average of the ascending or descending values for a latitude from the corresponding,

165   observed values of NO_2 at each longitude. In other words, the separate analyses of the ascending or

166   descending NO_2 in the LIMS Level 3 product do not account for likely diurnal variations in the NO_2.

167   Maximum ozone anomalies in Figs. 2a and 3a are nearly coincident with the center of the AH, again in

168   close agreement with the findings of R93 (their Figs. 2b and 2d). There is strong meridional transport of

169   air of relatively poor ozone along the western edge of the AH to across the Pole from 17 to 27 January.

170

171   Large-scale, zonal anomalies in HNO_3 (Figures 2d and 3d) are opposite in sign to those of GPH and

172   ozone. One exception is the relatively low values of HNO_3 near 80° N, 0° E on 17 January in Fig. 2d,

173   which has been interpreted as due to an uptake of gas phase HNO_3 onto PSC particles just upwind a day

174   or so earlier (Remsberg and Harvey, 2016). Yet, by 27 January (Fig. 3d) the cyclonic circulation about

175   the low GPH center indicates clearly that there must be net transport of low values of HNO_3 near 140° E,

176   along the axis of the polar night jet, across the Pole, and then to about 300° E. As a result, while both

177   ozone and NO_2 display the same wave 1 structures as the GPH field on 27 January, the HNO_3 distribution

178   exhibits quasi-wave 2 structure. Figs. 2c and 3c represent NO_2 anomalies from profiles of just the LIMS

179   V6 descending orbits, or from its nighttime values near 11 pm local time. Those anomalies for NO_2 are

180   from four zonal waves minus the zonal mean coefficient, rather than from six zonal waves as for all the

8

181   other LIMS Level 3 products. Most of the NO_x converts from NO to NO_2 at sunset, followed by a further,

182   partial conversion of the NO_2 to N_2O_5 up to the 11 pm observation time of LIMS (Brasseur and Solomon,

183   2005). The respective panels of Figs. 2 and 3 demonstrate that ozone and NO_2 have large-scale features

184   of opposite sign in the AH region, while HNO_3 and NO_2 have anomaly patterns of the same sign on 17

185   January but not on 27 January. Clearly, it is important to consider the amount of NO_x that is in the form

186   N_2O_5 in the AH region during that time span.

187

188   Figure 4 shows the zonal species variations from the V6 SE or Fourier coefficients at 31.6 hPa for 27

189   January at the latitude of 64˚ N and as calculated at grid points spaced every 5.625° of longitude. The

190   LIMS Fourier coefficients for each of the species are the result of applying the SE algorithm to their

191   Level 2 or profile data, as limited by the estimated data precisions. As a result, the V6 species variations

192   (black curves) are relatively accurate and significant, at least to the scale of zonal wave 6 (or to wave 4

193   for NO_2). Vertical error bars in Fig. 4 are the 2σ values from the error covariance matrix of the vector of

194   the V6 Fourier coefficients (Remsberg and Lingenfelser, 2010). Variations from the V5 data set at 30

195   hPa are included for comparison purposes (red curves).

196

197   HNO_3 within the polar vortex (0° to 90° E) is higher by nearly 2 ppbv compared to that in the AH region

198   (180° E to 240° E). Note from Fig. 3, however, that HNO_3 has a strong, positive Equator-to-Pole gradient

199   in the 0° to 90° E sector, whereas that of ozone is weak and slightly negative. Ozone in Fig. 4 has a

200   broad, wave 1 character, while HNO_3 exhibits two minima (at 130° E and 290° E). At 10 hPa and lower

201   pressures (or at higher z) a quasi-wave 2 structure is no longer apparent in HNO_3. Variations of the

202   descending and ascending (daytime or ~1:30 pm local time) NO_2 modes appear separately in Fig. 4.

203   Diurnal differences for NO_2 are seen only in the longitude sector from 320°E to 120˚ E, or across the

204   boundary of the cold polar vortex and the warmer AH region. Relatively low ozone in this region results

205   in only a slow conversion of NO_2 at sunset to NO_3 and finally to N_2O_5. Consequently, a larger fraction of

206   NO_x remains as NO_2 at the time of the LIMS descending mode observations, or ~11 pm local time. The

207   warmer AH region from 150° E to 270° E, on the other hand, has higher ozone mixing ratio, and the

208   decrease in NO_2 from its maximum at sunset is steeper, bringing NO_2 mixing ratios at the time of the

209   LIMS descending mode observation close to the value of the ascending mode measurement. There is

210   very little diurnal difference in NO_2 in that longitude region. Thus, air parcel history is important for

211   interpreting observed changes in the distributions of these two reactive species even in the AH region.

212   V5 NO_2 varies in a similar way, although its values are nearly twice those of V6.

213

4 Changing composition within the Aleutian High

215   Species variations with time are shown in Figure 5, as determined from the V6 orbital or Level 2 profiles

216   at 31.6 hPa and nearest to the center of the AH on each day and identified by the location of the maximum

217   GPH anomaly. Note that Fig. 5, which is analogous to Figure 7 of R93, also shows that the latitude of the

218   AH moves poleward from about 60° N to 68˚ N from 14 to 27 January. Its longitude moves slightly, too,

219   from 186˚ E on 14 January to 230˚ E on 19 January and then retreats partially to 214˚ E by 27 January.

220   Figure 6 illustrates those locations better as red boxes for each day. GPH of the 31.6-hPa level at the

221   center of AH grows from 23.0 to 23.8 km during that same time.

222

223   Vertical bars in Figure 5 represent root-sum-squared (RSS), single profile errors for 30 hPa (Remsberg et

224   al., 2007; 2009), and the ozone and H_2O variations are no greater than those error estimates of 15 %.

225   Those two species remain rather steady in the AH and are in keeping with their small horizontal gradients

226   on the 31.6-hPa surface and their relatively long chemical lifetimes. HNO_3 shows significant changes; it

227   declines from 10 to 8.2 ppbv from 14 to 18 January, but then increases rather steadily again to 10 ppbv by

228   27 January. Single profile RSS uncertainty for HNO_3 is ~8 % at 30 hPa (Remsberg et al., 2010).

10

229   Descending (or late evening) NO_2 declines from 1.1 to 0.5 ppbv from 15 to 19 January, increases to about

230   1.0 ppbv on 23 January, before declining again to 0.4 ppbv on 27 January. Ascending (early afternoon)

231   NO_2 is smaller than descending NO_2 from 14 to 17 January, or when the AH center is at about 60° N. As

232   the AH central latitude shifts northward after 17 January, both the ascending and descending NO_2 exhibit

233   similar values and indicate that the daytime observations are from near to or within the polar night

234   boundary. Generally, the RSS error for single NO_2 profiles is ~30 % at this pressure level, although

235   profile registration uncertainties can lead to larger errors across the polar night boundary. Remsberg et al.

236   (2010, their Fig. 3) showed an altitude-latitude plot of "zonal average NO_2" from only the descending (11

237   pm) orbital segments of 15 January, when the polar vortex is still nearly circular and centered on the Pole.

238   Its vertical distribution at 60° N declines from 2.5 ppbv at 20 hPa to a local minimum of < 1 ppbv at 35

239   hPa or about where the associated HNO_3 has its local maximum. In fact, the V6 retrieval algorithm sets

240   NO_2 to zero, when the forward radiance for the tangent layer approaches the measurement noise for that

241   channel (5.5×10^{-4} w-m^{-2}-sr^{-1}). Thus, the effect of a finite (~3.7 km) vertical resolution is to smooth

242   across that local NO_2 minimum, giving a high bias in its final retrieved value.

243

244   **5 Trajectory model with photochemistry**

245   In this section, we examine the interplay between photochemistry and dynamics during the evolution of

246   HNO_3 and NO_2 in the AH by making use of photochemical calculations along trajectories that terminate

247   in the AH region on 27 January. In these calculations, we use the V6 level 2 profile data to initialize the

248   air parcel composition, which allows a comparison between model results and co-located observations

249   along the trajectory in the AH region. The trajectory model is driven by 3-dimensional meteorological

250   data from MERRA (Rienecker et al., 2011) corresponding to January 1979. This dataset includes 3-

251   hourly information on surface pressure, horizontal wind, vertical pressure velocity, and temperature on a

252   1.25° longitude by 1.25° latitude grid. A family of 70 back trajectories is generated, with trajectories

11

253   beginning at 30 hPa from a grid of 2°-latitude by longitude covering a domain defined by 210° E and

254   218° E longitudes and 60° N and 86° N latitudes. The starting time of the back trajectories is 9 am GMT

255   (or 09Z) on 28 January, which corresponds to a local time of 11 pm on 27 January at 210° E. This is

256   close to the local time of LIMS descending mode observations in this latitude region. The selected region

257   overlaps the AH in the contour plot of V6 GPH anomalies for this day, as shown in Fig. 3b. The model

258   uses a 4th order Runge-Kutta advection scheme to generate 3-dimensional, kinematic back trajectories.

259   We save trajectory parameters required for further calculations on an hourly basis.

260

261   Figure 6 shows the back trajectory beginning on 27 January at 214° E, 68° N and 30 hPa. The numbers in

262   black along the trajectory represent the day numbers. Red colored squares with day numbers represent

263   the history of the location of the AH center at 31.6 hPa based on the maximum V6 GPH anomaly. This

264   V6 pressure level is the closest Level 2 value to 30 hPa. It is clear that between 22 and 27 January the

265   trajectory and the AH center remain in a region north of 54° N latitude, and the AH region provides an

266   isolated natural chemical laboratory for the constituents to evolve. Prior to 22 January the trajectory and

267   AH center diverge with the trajectory going backwards to latitudes as far south as 27° N. As we will

268   show later, the back trajectory beginning at 214° E and 60° N remains within the AH region or north of

269   45° N throughout the 10-day period. These differences among the trajectories affect their initial values

270   and the changes in air parcel composition.

271

272   We conducted time-dependent photochemical calculations along the trajectories in the forward direction.

273   Information used in these calculations include the vertical ozone column along the trajectories based on

274   V6 Level 3 ozone data, background sulfate aerosol surface area densities for January 1979 adopted from

275   the IGAC/SPARC CCMI recommendations for Reference Simulation 1 (Eyring et al., 2013), and solar

276   zenith angle corresponding to the local time of day. Aerosol surface area in the model is 4×10^{-9} cm^{-1} at

277   31 hPa and 60°N for January (see Table 1 of Hofmann and Solomon, 1989). The starting location and

278   mixing ratios of measured species are determined by identifying for each trajectory the spatially and

279   temporally closest LIMS descending mode observation between 14 and 17 January. Longitude separation

280   between the trajectory and the V6 data is within 15°, latitude separation within 7.5°, and time of

281   measurement within an hour. We use an updated version of the stratospheric diurnal photochemical

282   model (Natarajan and Callis, 1997), incorporating the chemical kinetics and photochemical data from the

283   recent JPL evaluation (Burkholder et al., 2015), to calculate the changes in the composition of the air

284   parcels until they reach the AH region on 27 January. Results from a time-dependent, 2-dimensional

285   chemistry-transport model (Callis et al., 1997) simulation corresponding to January 1979 provide

286   initialization estimates of other unmeasured HO_x, Cl_x, and NO_x species. The initialization procedure

287   involves repeated diurnal calculations at the fixed starting latitude, altitude, and day. During each diurnal

288   cycle, the mixing ratios of ozone, NO_2, and HNO_3 are set to the observed values at the local time of the

289   LIMS descending mode measurement (Natarajan et al., 2002). Within five diurnal cycles, the short-lived

290   chemical species reach near steady mixing ratios. Then, the photochemical model integration continues

291   along each trajectory until reaching the endpoint of 09Z on 28 January.

292

293   **6 Results and discussion**

294   We show in this section the results of sample trajectories that behave similar to those of the ensemble and

295   discuss the transformations occurring in the composition of the air parcels over their 10-day transit. All

296   trajectories terminate at 30 hPa but, since we use 3-dimensional kinematic trajectories based on MERRA,

297   there are fluctuations in pressure and altitude as the parcel moves along its trajectory. The length of

298   exposure to daylight also fluctuates and is not the same for all the trajectories. These differences certainly

299   affect the photochemical changes that occur.

300

13

301   Figure 7a shows, on a polar stereographic projection map of the Northern Hemisphere, three different

302   trajectories terminating at a longitude of 214° E. The latitude circles in the figure are 10° apart and

303   poleward of 20° N. The uppercase letters A, B, and C denote the starting location of the trajectories and

304   the lowercase letters a, b, and c mark the endpoints at 60° N, 72° N, and 80° N latitude, respectively. The

305   color scale ranging from 0 to 1 represents the accumulated hours of exposure to darkness along each

306   trajectory expressed as a fraction of the total length of the trajectory in hours. The cumulative fraction of

307   darkness at the endpoint is 0.70, 0.67, and 0.63 for the trajectories A-a, B-b, and C-c, respectively. Fig.

308   7b shows the same three trajectories but now color-coded to demonstrate the calculated variation of

309   HNO_3. Trajectory A-a starts at 222.1° E and 59.9° N on 17 January with an initial HNO_3 mixing ratio of

310   9.05 ppbv, adopted from the nearby LIMS observation. Both the starting and termination points for this

311   trajectory are very near the center of the AH as seen in the GPH anomaly contours (Fig. 3b). The mixing

312   ratio of HNO_3 increases to 10.8 ppbv, mostly due to the heterogeneous hydrolysis involving N_2O_5 and

313   sulfate aerosol. This conversion of NO_x predominates while the parcel is in darkness.

314

315   Figure 8a shows the variation with time of selected chemical constituents as the air parcel moves along

316   trajectory A-a. Shown by the thick broken line at the top of the figure are the segments when the parcel

317   along this trajectory is in darkness. It is clear that HNO_3 increases during extended periods of darkness,

318   which occur more often when the parcel traverses through higher latitudes. This increase in HNO_3 comes

319   at the expense of other reactive nitrogen species as can be seen in the decrease in the mean value and

320   somewhat diminished amplitude of the diurnal variation of NO_2. There is also a dampening of the diurnal

321   variation of N_2O_5 because of limited exposure to sunlight, although its mean value remains higher. The

322   daytime peak mixing ratio of NO is low (not shown). When a trajectory is at lower latitudes (e.g.,

323   between 17 and 22 January), all NO_x species display larger diurnal variations with little change in mean

324   value. HNO_3 also shows some diurnal fluctuations due to daytime photolysis followed by production due

14

325 to heterogeneous chemistry in darkness and with a slight overall increase in mean mixing ratio. After 22

326 January, the air parcel moves to higher latitudes and experiences extended periods of darkness, leading to

327 the steady increase in HNO_3. Thus, a combination of dynamics, which determines the trajectory that the

328 parcel follows, and both gas-phase and heterogeneous photochemistry explains the higher levels of HNO_3

329 measured by LIMS near 30 hPa in the AH region on 27 January. Ozone, which has a longer chemical

330 lifetime at this pressure level, shows almost no change. However, we also note that at lower pressures,

331 e.g., at 5 hPa, there is a similar impact of dynamics and photochemistry in the formation of pockets of low

332 ozone mixing ratio within the AH region during winter (Manney et al., 1995; Morris et al., 1998; Harvey

333 et al., 2004). The photochemical time constant for ozone at those pressure levels is short enough that air

334 parcels originating from lower latitudes and containing higher ozone go through a chemical

335 transformation, when confined for an extended period of time within the AH region. This results in a

336 destruction of ozone in reaching photochemical equilibrium under daylight conditions. Conversely, the

337 increase in HNO_3 at 30 hPa is due mainly to the nighttime heterogeneous chemistry.

338

339 In order to highlight the role of the heterogeneous reactions involving background sulfate aerosols, we

340 have repeated the photochemical calculations along the same trajectories but considering only gas-phase

341 reactions. Fig. 8b shows the mixing ratios in this case for trajectory A-a. HNO_3 decreases from the initial

342 mixing ratio of 9.1 ppbv and settles to a value closer to 8.0 ppbv by 20 January. Because we initialized

343 the parcel using LIMS HNO_3 data, that initial drop is indicative of the imbalance created by removing the

344 source due to heterogeneous conversion. Small diurnal fluctuations are apparent during the passage

345 through lower latitudes because of photolysis, but they are nearly absent when the parcel is in the high

346 latitude region. Without heterogeneous reactions, N_2O_5 remains the primary reservoir of NO_x during the

347 nighttime and reaches its peak values just when the parcel is about to emerge from darkness. The mean

348 mixing ratio of N_2O_5 is about 2 ppbv between 23 and 25 January, when the parcel experiences that

349   extended period of darkness at high latitude. The diurnal cycle for NO_2 exhibits larger amplitudes when

350   using only gas-phase reactions, since the absence of additional production of HNO_3 keeps the NO_x mixing

351   ratio higher. The difference in the mixing ratio of HNO_3 in the AH region between the two simulations

352   shows the impact of heterogeneous reactions in the partitioning of odd nitrogen. While the agreement for

353   HNO_3 between model and the LIMS data of Fig. 5 is good with the inclusion of heterogeneous reactions,

354   the comparison for NO_2 is worse; the model gives mixing ratios that are lower than the measurement.

355   But, that is also when the V6 NO_2 in the AH region is near its local minimum of about 0.5 ppbv, and we

356   noted in Section 4 that such small retrieved values are likely to have a high bias.

357

358   Trajectory B-b, shown in Fig. 7a, starts from 173.3° E and 23° N on 14 January. After spending a few

359   days in the lower latitudes, the air parcel along this trajectory takes a nearly meridional path to the AH

360   region. During the last 5 days the parcel remains confined in the AH region, similar to the parcel along

361   trajectory A-a. The chemical evolution along the trajectory, shown in Fig. 9a, is also similar to that along

362   trajectory A-a displayed in Fig. 8a. Large diurnal variations in NO_2 and N_2O_5 occur during the initial

363   period between 14 and 20 January, when the trajectory is in the lower latitudes. Even HNO_3 displays

364   noticeable variations with an increase during night caused by the heterogeneous conversion of N_2O_5

365   followed by a decrease due to photolysis during daytime. Amplitudes of the diurnal variations diminish

366   in the high latitude AH region, due to reduced photolytic loss, especially for HNO_3, during the shorter

367   daylight period and at higher zenith angles. The corresponding increase in the nighttime heterogeneous

368   conversion leads to HNO_3 mixing ratios greater than 10 ppbv at the end of the trajectory. Between 22 to

369   25 January, NO_2 displays a steady diurnal cycle, while N_2O_5 shows a declining peak value. The increase

370   in HNO_3 does not occur with a corresponding decrease in NO_2. During extended periods of darkness,

371   NO_2 decreases to a negligible amount as shown at the end of the trajectory on 27 January. When there are

372   only gas phase reactions, the variation of HNO_3 is as shown by the red line. Again, initialization of the

373   photochemical model uses the V6 data, and the absence of heterogeneous reactions introduces an

374   imbalance leading to the negative tendency in HNO_3.

375

376   Trajectory C-c, shown in Fig. 7a, starts from 79.9° E and 27.6° N on 17 January. Until 24 January, this

377   parcel stays south of 40° N and then takes a meridional path directly northward reaching 80° N by 28

378   January. This is slightly north of the AH but still outside the polar vortex. Fig. 9b shows variations of the

379   species mixing ratios along the trajectory C-c for the simulation with heterogeneous chemistry. HNO_3

380   mixing ratio at the beginning of the trajectory (C) is about 7.8 ppbv, and it increases to about 8.7 ppbv at

381   the endpoint (c). Measurements in Fig. 3d indicate a quasi-wave 2 feature in HNO_3 at 31.6 hPa, with

382   peak values in the polar vortex region and AH. The minimum in HNO_3 between these two regions is a

383   result of the rapid transit of air parcels from lower latitude along trajectories similar to C-c. The air

384   parcels remain in the low latitudes for a longer time, and photolysis during daylight hours keeps the net

385   change in HNO_3 low. Only later is there a noticeable increase in HNO_3 for the high latitude segment of

386   the trajectory. NO_2 and N_2O_5 display diurnal variations as expected in the middle latitudes. After 21

387   January, there is a decrease occurring in the peak value of NO_2 at every successive sunset along the

388   trajectory. The corresponding minimum in N_2O_5 shows a small increasing trend especially after 24

389   January, and this is due to the increasing lifetime against photolysis at winter high latitudes. The parcel is

390   in complete darkness during the last 24 hours, when NO_2 continuously decreases to a very low mixing

391   ratio, N_2O_5 declines slowly, and HNO_3 increases.

392

393   Figure 10 shows HNO_3 mixing ratios calculated on a longitude-latitude grid for the end time of the

394   ensemble of 70 trajectories, corresponding to 09Z on 28 January. The latitudinal variation in HNO_3

395   between 60° N in the AH region and the Pole clearly shows a dip to lower values near 80° N in the model

396   calculations. This spatial distribution occurs even when heterogeneous reactions are not included.

17

397   However, calculations with heterogeneous chemistry simulate the magnitude of the LIMS HNO$_3$

398   observations better. Combined with the higher HNO$_3$ values in the polar vortex (not a focus of this

399   paper), the differing trajectories explain the formation of a quadrupole structure at 30 hPa seen in the

400   LIMS HNO$_3$ observations during the minor warming. As reported by R93, this feature is present in the

401   LIMS V5 data also, except that V5 HNO$_3$ is nearly of the same magnitude in the AH and the polar vortex

402   at 30 hPa on 27 January. For the same conditions, the V6 HNO$_3$ is larger in the polar vortex than in the

403   AH by about 2 ppbv.

404

405   Even though we have shown and discussed the model results for only three of the trajectories, all of

406   which end along 214° E longitude, the results for the entire ensemble provide a consistent picture. Figure

407   11a is a scatter plot of the calculated HNO$_3$ along the 70 trajectories versus the spatially and temporally

408   closest LIMS observations. Differences between the model and LIMS data are of the order of the RSS

409   error of 0.8 ppbv, except for mixing ratios greater than 10 ppbv where the model values are higher.

410   Figure 11b is a similar scatter plot for NO$_2$; model values are lower than the V6 observations that have an

411   RSS error of 0.24 ppbv. Deviations from the diagonal dashed line for both HNO$_3$ and NO$_2$ could be due

412   to a variety of factors, in addition to bias errors of the data. The criteria we used for selecting the closest

413   observation are coarse, but tightening those criteria reduces the amount of data available for initializing

414   the model and for comparison along the trajectory. While we used the closest LIMS observation to

415   constrain the initialization of the model, other unmeasured species as well as total odd nitrogen are from

416   two-dimensional model output that introduces some uncertainty. We have used the recommended kinetic

417   rate constants, but any uncertainty in key reaction rates could affect the calculated variations in the

418   composition. Another possible source of error is the background stratospheric aerosol, surface area

419   density. We used the climatology from IGAC/SPARC CCMI database, which is zonally averaged data.

420   There were no major volcanic perturbations in late 1978 and early 1979, so large perturbations from this

421 database are most unlikely. While at the lower latitudes photolysis during the daylight hours is important

422 in limiting the impact of heterogeneous reactions, the aerosol data directly affects that rate of conversion

423 of N_2O_5 to HNO_3. It may be that background aerosols in the vortex at high latitudes are less abundant

424 than prescribed, which could explain the apparent high bias in model HNO_3 in Figure 11a for values

425 greater than 10 ppbv. Although LIMS did not measure N_2O_5, analyses involving ATMOS measurements

426 show clearly the role of N_2O_5 and heterogeneous reactions in the stratospheric odd nitrogen chemistry

427 (Natarajan and Callis, 1991). A more comprehensive study of the changes in atmospheric composition in

428 the AH region using data from more recent satellite experiments is beyond the scope of this study.

429

430 **7 Seasonal evolution of PV, HNO_3, H_2O, and NO_2**

431 Anticyclone features usually develop in the Northern Pacific stratosphere and are present about 60 % of

432 the time during winter (Harvey and Hitchman, 1996; Baldwin and Holton, 1988). Therefore, we place the

433 V6 species variations of 14-27 January into the broader context of their seasonal variations. As before,

434 one can ignore the effects of any remnants from PSCs for the species away from the polar winter vortex.

435 First, Figure 12 is a time series plot of the dynamical tracer, PV, on the isentropic surface of 550 K (near

436 31.6 hPa) for 25 October 1978 through 28 May 1979.

437   $PV \; = \; (f + \zeta) / \sigma \;\;,$ (1)

438 where $f = 2\Omega \sin \varphi$ is the local vertical component of the planetary vorticity on a pressure surface and $\zeta =$

439 $(r \cos \varphi)^{-1} (\partial v/\partial \lambda - \partial(u \cos \varphi)/\partial \varphi)$ is the relative vorticity in polar coordinates (longitude λ and latitude φ).

440 σ is isentropic density (kg m^{-2} K^{-1}) and $1/\sigma = -g\, \partial\theta/\partial p = (1/\rho)\, \partial\theta/\partial z$ is static stability. Geostrophic wind

441 components, u and v, are calculated at grid points from the V6 GPH fields. Then, daily values of the

442 vertical component of PV are computed at each grid point from the zonal and meridional components of

443 the wind (u and v), plus the local vertical gradients of potential temperature versus pressure from V6,

19

444   following Harvey et al. (2009). The ordinate of Fig. 12 is in terms of equivalent latitude φ from the Pole

445   (90˚) to 15˚ N and is from a monotonic ordering of the daily PV from high values inside the polar vortex

446   to lower values outside (see e.g., Butchart and Remsberg, 1986). Thus, equivalent latitude is a vortex-

447   centered coordinate that assigns the highest PV values (located in the center of the vortex) to be at 90° N.

448   Tic marks along the abscissa denote the middle of each month, and the PV time series have a seven point

449   smoothing. The ordinate is linear in φ to accentuate variations in the PV field at high equivalent latitudes.

450   The effects of the AH on the displacement and erosion of the PV vortex during 14-27 January are in Fig.

451   12 from φ of about 60° to 90° and following the tic mark labeled 01 on the abscissa.

452

453   The effect of the AH in peeling away material contours from the edge of the polar vortex has been

454   described aptly (e.g., McIntyre, 1995; Juckes and McIntyre, 1987; Rose, 1986). Fig. 12 indicates the

455   continual erosion of highest PV values during late winter and early spring due to zonal planetary wave 1

456   (the AH) and wave 2 activity. The adjacent "surf zone" region of lower PV values expands and exhibits

457   weakened gradients (φ ~ 30° to 60°) from the meridional mixing of PV across both the lower and higher

458   latitudes (McIntyre and Palmer, 1983). It is also noted that the vortex was split (wave-2) at four separate

459   times at the level of 31.6 hPa: late October, late November/early December, late February, and in early

460   April. Both scales of zonal forcing are indicative of the effects of planetary wave activity as it propagates

461   from the troposphere to the 31.6-hPa level (Juckes and O'Neill, 1988) and/or of a poleward eddy heat flux

462   (Colucci and Ehrmann, 2018). The meridional gradient of PV is quite weak equatorward of φ ~ 60˚ N in

463   winter and then across all latitudes by mid-April, or after the polar vortex has undergone significant

464   erosion. The large-scale anticyclones and associated zonal easterlies expand toward the middle latitudes

465   by April.

466

467   Figure 13 shows the corresponding HNO_3 distribution, as determined by averaging HNO_3 values around

468   the daily PV contours and then ordering them according to the φ of Fig. 12. Those averages represent

469   approximate, modified Lagrangian mean (MLM) values for HNO_3 or its average values around the PV

470   contours, and they enable one to identify differences in behavior (e.g., chemical changes) for trace

471   constituents versus PV (McIntyre, 1980; Butchart and Remsberg, 1986). HNO_3 varies nearly

472   monotonically with latitude at this level, and values as high as 13 ppbv are found near the center of the

473   vortex (φ = 90˚) by late November and during the polar night. Such high values indicate a nearly

474   complete chemical conversion of the available NO_y to its reservoir component HNO_3. Poleward of about

475   φ = 70˚ the HNO_3 contours are aligned well with those of PV, indicating that HNO_3 is an excellent tracer

476   at 550 K, particularly in winter polar night when further chemical changes are inefficient. However, there

477   should be some HNO_3 uptake into PSCs, when temperatures become cold enough.

478

479   A sequence of polar orthographic plots (not shown) indicates that there is a buildup of HNO_3 inside the

480   polar vortex in November, punctuated by meridional transport during the zonal wave 1 events of early

481   December and in January, and then followed by a splitting of the vortex in mid to late February. There is

482   significant transport of HNO_3 from the polar region to middle equivalent latitudes (φ = 45 to 20˚) during

483   those events. Meridional gradients of HNO_3 are larger in winter at both φ of 70˚ and near 20°, marking

484   the polar and subtropical edges of the region of efficient meridional mixing. The subtropical boundary of

485   the so-called "tropical pipe" region shifts from φ = 25˚ to about 15˚ from early December to late January

486   and then remains at that location into springtime (Remsberg and Bhatt, 1996). There is erosion of the

487   high HNO_3 values of the polar vortex by early March. Thereafter, HNO_3 decreases at all equivalent

488   latitudes, due to the daily effects of the chemical re-partitioning of NO_y away from HNO_3 and toward NO

489   and NO_2 under sunlit conditions.

21

490

491   Figure 14 displays the time series plot of the MLM for V6 H_2O, a better tracer of stratospheric transport.

492   Relatively large values of 5.5 to 6.0 ppmv occur at high latitudes from mid-November to early January

493   and indicate the effects of the slow descent of higher values within the vortex. H_2O is higher in the upper

494   stratosphere from the oxidation of methane. Elevated H_2O values at $\varphi > 75°$ on 13-15 and 19 January are

495   due to residual emissions from PSCs. However, values of ~7 ppmv also appear in early February to mid-

496   March, when temperatures are much too warm for the existence of PSCs. Although those higher values

497   are within the uncertainties for retrieved H_2O, they compare well with times when there is descent of

498   higher ozone values in response to the major stratospheric warmings (c.f., Fig. 18 in Leovy et al., 1985).

499

500   Finally, Figure 15 is the MLM plot of V6 NO_2, based on only its profiles along descending (nighttime)

501   orbital segments. Smallest values of NO_2 occur in the polar vortex in late November and early December,

502   when the HNO_3 values of Fig. 13 reach 13 ppbv. As with H_2O, there are several minor increases in NO_2

503   at the highest latitudes in mid-January, and they occur at locations of residual effects from PSCs. The

504   excess values of NO_2 poleward of $\varphi = 75°$ in February occur where the variations of PV in Fig. 12 also

505   indicate the effects of transport and where there may have been descent of higher NO_2 values within the

506   vortex (Holt et al., 2012). The distribution of NO_2 away from the vortex varies more slowly and

507   smoothly. Fig. 12 also indicates that there is considerable mixing for PV at $\varphi \sim 60°$ to $75°$ during

508   February, and Fig. 15 shows that NO_2 is increasing along the PV contours. The vortex split into two

509   sectors in the middle stratosphere from mid to late February, when there was transport and descent of air

510   having higher NO_2 values at the high latitudes. NO_2 increases steadily from March to May, due to the

511   conversion of HNO_3 to NO_2 upon the return of sunlight.

512

513   There are significant seasonal variations of NO_2 displayed in Fig. 15 at middle equivalent latitudes. The

514   re-partitioning of the NO_y species to HNO_3 occurs in the presence of background aerosols from late

515   autumn to winter, followed by photochemical conversion of the HNO_3 vapor back to NO_2 in springtime

516   (e.g., Austin et al., 1986). Fig. 15 shows that the very low values of NO_2 extend from near the Pole to at

517   least $\varphi = 30°$ in early December, and then retreat toward higher latitudes by late February. This variation

518   of the NO_2 time series is an indicator of the so-called "Noxon cliff" feature of stratospheric column NO_2

519   during winter (e.g., Noxon, 1979).

520

521   **8 Conclusions**

522   A significant improvement of the LIMS data set from V5 to V6 is the better accuracy of the retrieved V6

523   NO_2 profiles. Both the V6 HNO_3 and NO_2 are of good quality, at least to within their respective error

524   estimates and away from very cold regions of the vortex and their PSC remnants. The V6 species data are

525   evaluated further in terms of the consistency of the HNO_3 and NO_2 distributions in the AH region during

526   the minor warming event that took place in January 1979. In an earlier analysis of the LIMS V5 data,

527   R93 highlighted an increase for HNO_3 at 30 hPa within the AH region but with little change in NO_2, and

528   they suggested the need for some unknown process leading to the production of HNO_3 and to the

529   development of the quasi-wave 2 signature in its zonal distribution. The present study considers

530   photochemical model calculations along kinematic trajectories over a 10-day period that terminate in the

531   AH region on 28 January. The results indicate that there was an increase of about 2 ppbv in HNO_3 and a

532   decrease of order 0.5 ppbv in NO_2, mainly as a result of heterogeneous reactions converting N_2O_5 on

533   surfaces of background stratospheric sulfuric acid aerosols. R93 and Considine et al. (1992) alluded to

534   this mechanism but reported that their three- and two-dimensional model studies with heterogeneous

535   chemistry gave results that still did not agree well with the LIMS V5 species. On the contrary, the

536 latitudinal variations of HNO_3 at the end of our Lagrangian trajectory calculations agree reasonably with

537 the LIMS V6 data. Those variations depend on the initial conditions and the extent of exposure of air

538 parcels to sunlit and dark conditions, and hence on the dynamically controlled histories of the separate

539 trajectories. Our model calculations also reveal the formation of a dip in observed HNO_3 mixing ratios

540 north of the AH, due to meridional transport of low latitude air across the Pole. Therefore, we conclude

541 that the study approach of R93 was valid and should have led them to better comparisons, if the V6 data

542 set had been available earlier.

543

544 When the effects of heterogeneous chemistry are included in the model calculations, the variations of

545 HNO_3 and NO_2 along trajectories agree more reasonably with the LIMS V6 observations in the relatively

546 isolated AH region. Yet, the model still underestimates NO_2 compared to the V6 values along some

547 trajectory paths. A part of those differences may be due to an inability to retrieve a local minimum in the

548 V6 NO_2 profile with good accuracy, at least based on the finite, vertical field of view of the NO_2 channel

549 radiances and their associated LIMS temperature profiles. Still, the present study demonstrates that a

550 combination of dynamical and photochemical changes can explain the maximum mixing ratios of HNO_3

551 in both the AH region and at the winter polar vortex, plus its lower values around the periphery of both

552 circulation systems. HNO_3 re-partitions by photochemistry toward NO_2 from winter to springtime, when

553 the anticyclone regions extend to middle latitudes. We also present examples of the seasonal evolution of

554 HNO_3 and NO_2 during 1978-1979 as a separate aspect of the V6 data set for the validation of

555 chemistry/climate models of the middle to lower stratosphere.

556

561 **References**

562 Austin, J. A., Garcia, R. R., Russell III, J. M., Solomon, S., and Tuck, A. F.: On the atmospheric

563 photochemistry of nitric acid, J. Geophys. Res., 91, 5477-5485, 1986.

564

565 Baldwin, M. P., and Holton, J. R.: Climatology of the stratospheric polar vortex and planetary

566 wave breaking, J. Atmos. Sci., 45, 1123-1142, 1988.

567

568 Brasseur, G. P. and Solomon, S.: Aeronomy of the middle atmosphere, 3rd Edition, Springer, The

569 Netherlands, 644 pp., 2005.

570

571 Burkholder, J. B., Sander, S. P., Abbatt, J., Barker, J. R., Huie, R. E., Kolb, C. E., Kurylo, M. J.,

572 Orkin, V. L., Wilmouth, D. M., and Wine, P. H.: Chemical kinetics and photochemical data for

573 use in atmospheric studies, Evaluation No. 18, JPL Publication 15-10, Jet Propulsion Laboratory,

574 Pasadena, 2015, http://jpldataeval.jpl.nasa.gov.

575

576 Butchart, N. and Remsberg, E. E.: The area of the stratospheric polar vortex as a diagnostic for

577 tracer transport on an isentropic surface, J. Atmos. Sci., 43, 1319-1339, 1986.

578

579 Callis, L. B., Natarajan, M., Lambeth, J. D., and Boughner, R. E.: On the Origin of Midlatitude

580 Ozone Changes: Data Analysis and Simulations for 1979 -1993, J. Geophys. Res., 102, 1215-

581 1228, 1997.

582

583

584 Colucci, S. J., and Ehrmann, T. S.: Synoptic-dynamic climatology of the Aleutian High, J.

585 Atmos. Sci., 75, 1271-1283, doi:10.1175/JAS-D-17-0215.1, 2018.

586

587 Considine, D. B., Douglass, A. R., and Stolarski, R. S.: Heterogeneous conversion of N_2O_5 to

588 HNO_3 on background stratospheric aerosols: comparisons of model results with data, Geophys.

589 Res. Lett., 19, 397-400, 1992.

590

591 Eyring, V., Lamarque, J.-F., Hess, P., Arfeuille, F., Bowman, K., Chipperfield, M. P., Duncan,

592 B., Fiore, A., Gettelman, A., Giorgetta, M. A., Granier, C., Hegglin, M., Kinnison, D., Kunze,

593 M., Langematz, U., Luo, B., Martin, R., Matthes, K., Newman, P. A., Peter, T., Robock, A.,

594 Ryerson, T., Saiz-Lopez, A., Salawitch, R., Schultz, M., Shepherd, T. G., Shindell, D., Staehelin,

595 J., Tegtmeier, S., Thomason, L., Tilmes, S., Vernier, J.-P., Waugh, D. W., and Young, P. J.:

596 Overview of IGAC/SPARC chemistry-climate model initiative (CCMI) community simulations

597 in support of upcoming ozone and climate assessments, SPARC Newsletter No. 40, January,

598 2013.

599

600 Gille, J. C. and Russell III, J. M.: The limb infrared monitor of the stratosphere: experiment

601 description, performance, and results, J. Geophys. Res., 89, 5125-5140, 1984.

602

603 Harvey, V. L. and Hitchman, M. H.: A climatology of the Aleutian High, J. Atmos. Sci., 53,

604 2088-2101, 1996.

605

606 Harvey, V. L., Pierce, R. B., Hitchman, M. H., Randall, C. E., and Fairlie, T. D.: On the

607 distribution of ozone in stratospheric anticyclones, J. Geophys. Res., 109, D24308,

608 doi:10.1029/2004JD004992, 2004.

609

610 Harvey, V. L., Randall, C. E., and Hitchman, M. H.: Breakdown of potential vorticity-based

611 equivalent latitude as a vortex-centered coordinate in the polar winter mesosphere, J. Geophys.

612 Res., 114, D22105, doi:10.1029/2009JD012681, 2009.

613

614 Hofmann, D. J., and Solomon, S.: Ozone destruction through heterogeneous chemistry following

615 the eruption of El Chichon, J. Geophys. Res., 94, D4, 5029-5041, 88JD04231, 1989.

616

617 Holt, L. A., Randall, C. E., Harvey, V. L., Remsberg, E. E., Stiller, G. P., Funke, B., Bernath, P.

618 F., and Walker, K. A.: Atmospheric effects of energetic particle precipitation in the Arctic winter

619 1978-1979 revisited, J. Geophys. Res., 117, D05315, doi:10.1029/2011JD016663, 2012.

620

621 Juckes, M. N., and McIntyre, M. E.: A high-resolution one-layer model of breading planetary

622 waves in the stratosphere, Nature, 328, 590-596, 1987.

623

624 Juckes, M. N., and O'Neill, A.: Early winter in the northern stratosphere, Quart. J. R. Meteorol.

625 Soc., 114, 1111-1125, 10.1002/qj.49711448211, 1988.

626

627   Lambert, A., Santee, M. L., Wu, D. L., and Chae, J. H.: A-train CALIOP and MLS observations

628   of early winter Antarctic polar stratospheric clouds and nitric acid in 2008, Atmos. Chem. Phys.,

629   12, 2899-2931, doi:10.5194/acp-12-2899-2012, 2012.

630

631   Leovy, C. B., Sun, C.R., Hitchman, M. H., Remsberg, E. E., Russell III, J. M., Gordley, L. L.,

632   Gille, J. C., and Lyjak, L. V.: Transport of ozone in the middle stratosphere: evidence for

633   planetary wave breaking, J. Atmos. Sci., 42, 230-244, 1985.

634

635   Manney, G. L., Froidevaux, L., Waters, J. W., Zurek, R. W., Gille, J. C., Kumer, J. B.,

636   Mergenthaler, J. L., Roche, A. E., O'Neill, A., and Swinbank, R.: Formation of low-ozone

637   pockets in the middle stratospheric anticyclone during winter, J. Geophys. Res., 100, D7, 13,939-

638   13,950, 1995.

639

640   McIntyre, M. E.: Towards a Lagrangian-mean description of stratospheric circulations and

641   chemical transport, Phil. Trans. R. Soc. London, A296, 129-148, 1980.

642

643   McIntyre, M. E.: The stratospheric polar vortex and sub-vortex: fluid dynamics and midlatitude

644   ozone loss, Phil. Trans. R. Soc. London, A352, 227-240, 1995.

645

646   McIntyre, M. E. and Palmer, T. N.: Breaking planetary waves in the stratosphere, Nature, 305,

647   593-600, 1983.

648

649   Morris, G. A., Kawa, S. R., Douglass, A. R., Schoeberl, M. R., Froidevaux, L., and Waters, J.:

650   Low-ozone pockets explained, J. Geophys. Res., 103, D3, 3599-3610, 1998.

651

652   Natarajan, M. and Callis, L. B.: Stratospheric photochemical studies with Atmospheric Trace

653   Molecule Spectroscopy (ATMOS) measurements, J. Geophys. Res., 96, D5, 9361-9370,

654   doi:10.1029/91JD00290, 1991.

655

656   Natarajan, M. and Callis, L. B.: Ozone variability in the high latitude summer stratosphere,

657   Geophys. Res. Lett., 24, no. 10, 1191-1194, 1997.

658

659   Natarajan, M., Remsberg, E. E., and Gordley, L. L.: Ozone budget in the upper stratosphere:

660   model studies using the reprocessed LIMS and the HALOE datasets, Geophys. Res. Lett., 29, no.

661   7, doi:10.1029/2001GL014262, 2002.

662

663   Noxon, J.: Stratospheric NO_2, 2. global behavior, J. Geophys. Res., 84, no. C8, 5067-5076, 1979.

664

665   Remsberg, E. E., and Bhatt, P. P.: Zonal variance of nitric acid vapor as an indicator of

666   meridional mixing in the subtropical lower stratosphere, J. Geophys. Res., 101, 29,523-29,530,

667   1996.

668

669   Remsberg, E. and Harvey, V. L.: Effects of polar stratospheric clouds in the Nimbus 7 LIMS

670   Version 6 data set, Atmos. Meas. Tech., 9, 2927-2946, doi:10.5194/amt-9-2927-2016, 2016.

671

Remsberg, E. and Lingenfelser, G.: LIMS Version 6 Level 3 dataset, NASA/TM-2010-216690,

available at http://www.sti.nasa.gov (last access: 6 May 2015), 13 pp., 2010.

674

Remsberg, E. E., Bhatt, P. P., Eckman, R. S., Gordley, L. L., Russell III, J. M., and Siskind, D.

E.: Effect of the HITRAN 92 spectral data on the retrieval of NO_2 mixing ratios from Nimbus 7

LIMS, J. Geophys. Res., 99, D11, 22,965-22,973, 94JD02042, 1994.

678

Remsberg, E. E., Gordley, L. L., Marshall, B. T., Thompson, R. E., Burton, J., Bhatt, P., Harvey,

L. V., Lingenfelser, G., and Natarajan, M.: The Nimbus 7 LIMS version 6 radiance conditioning

and temperature retrieval methods and results, J. Quant. Spectros. Rad. Transf., 86, 395-424,

doi:10.1016/j.jqsrt.2003.12.007, 2004.

683

Remsberg, E., Lingenfelser, G., Natarajan, M., Gordley, L., Marshall, B. T., and Thompson, E.:

On the quality of the Nimbus 7 LIMS version 6 ozone for studies of the middle atmosphere, J.

Quant. Spectros. Rad. Transf., 105, 492-518, doi:10.1016/j.jqsrt.2006.12.005, 2007.

687

Remsberg, E. E., Natarajan, M., Lingenfelser, G. S., Thompson, R. E., Marshall, B. T., and

Gordley, L. L.: On the quality of the Nimbus 7 LIMS Version 6 water vapor profiles and

distributions, Atmos. Chem. Phys., 9, 9155-9167, https://doi.org/10.5194/acp-9-9155-2009,

2009.

692

31

693 Remsberg, E., Natarajan, M., Marshall, B. T., Gordley, L. L., Thompson, R. E., and

694 Lingenfelser, G.: Improvements in the profiles and distributions of nitric acid and nitrogen

695 dioxide with the LIMS version 6 dataset, Atmos. Chem. Phys., 10, 4741-4756, doi:10.5194/acp-

696 10-4741-2010, 2010.

697

698 Remsberg, E., Natarajan, M., Fairlie, T. D., Wargan, K., Pawson, S., Coy, L., Lingenfelser, G.,

699 and Kim, G.: On the inclusion of Limb Infrared Monitor of the Stratosphere version 6 ozone in a

700 data assimilation system, J. Geophys. Res., 118, 7982-8000, doi:10.1002/jgrd.50566, 2013.

701

702 Rienecker, M.M., Suarez, M. J., Gelaro, R., Todling, R., Bacmeister, J., Liu, E., Bosilovich, M.

703 G., Schubert, S. D., Takacs, L., Kim, G.-K., Bloom, S., Chen, J., Collins, D., Conaty, A., da

704 Silva, A., Wei G., Joiner J. , Koster R. D., Lucchesi, R., Molod, A., Owens, T., Pawson, S.,

705 Pegion, P., Redder, C. R., Reichle, R., Robertson, F. R., Ruddick, A. G., Sienkiewicz, M., and

706 Woollen, J.: MERRA: NASA's Modern-Era Retrospective Analysis for Research and

707 Applications. J. Climate, 24, 3624-3648, doi:10.1175/JCLI-D-11-00015.1, 2011.

708

709 Rodriguez, J. M., Ko, M. K. W., and Sze, N. D.: Role of heterogeneous conversion of N_2O_5 on

710 sulfate aerosols in global ozone losses, Nature, 352, 134-137, doi:10.1038/352134a0, 1991.

711

712 Rood, R. B., Kaye, J. A., Nielsen, J. E., Schoeberl, M. R., and Geller, M. A.: Nitric acid forecast

713 experiments, Physica Scripta, 36, 337-354, 1987.

714

715 Rood, R. B., Douglass, A. R., Kaye, J. A., and Considine, D. B.: Characteristics of wintertime

716 and autumn nitric acid chemistry as defined by limb infrared monitor of the stratosphere (LIMS)

717 data, J. Geophys. Res., 98, 18,533-18,545, 1993.

718

719 Rose, K.: The stratospheric winter polar vortex simulated as a material entity, J. Atmos. Terr.

720 Phys., 48, 1197-1202, 1986.

721

722 SPARC: The SPARC Data Initiative: Assessment of stratospheric trace gas and aerosol

723 climatologies from satellite limb sounders. M. I. Hegglin and S. Tegtmeier (Eds.), SPARC

724 Report No. 8, WCRP-05/2017, doi:10.3929/ethz-a-010863911, available at www.sparc-

725 climate.org/publications/sparc-reports/, 2017.

726

727 Shepherd, T. G., Plummer, D. A., Scinocca, J. F., Hegglin, M. I., Fioletov, V. E., Reader, M. C.,

728 Remsberg, E., von Clarmann, T., and Wang, H. J.: Reconcilation of halogen-induced ozone loss

729 with the total-column ozone record, Nature Geoscience, 7, 443–449, doi:10.1038/ngeo2155,

730 2014.

731

732 Stolarski, R. S., Douglass, A. R., Remsberg, E. E., Livesey, N. J., and Gille, J. C.: Ozone

733 temperature correlations in the upper stratosphere as a measure of chlorine content, J. Geophys.

734 Res., 117, D10305, doi:10.1029/2012JD017456, 2012.

735

736   Tegtmeier, S., Hegglin, M. I., Anderson, J., Bourassa, A., Brohede, S., Degenstein, D.,

737   Froidevaux, L., Fuller, R., Funke, B., Gille, J., Jones, A., Kasai, Y., Krüger, K., Kyrölä, E.,

738   Lingenfelser, G., Lumpe, J., Nardi, B., Neu, J., Pendlebury, D., Remsberg, E., Rozanov, A.,

739   Smith, L., Toohey, M., Urban, J., von Clarmann, T., Walker, K. A., Wang, R. H. J.: SPARC

740   Data Initiative: A comparison of ozone climatologies from international satellite limb sounders,

741   J. Geophys. Res., 118, 12,229–12,247, doi:10.1002/2013JD019877, 2013.

742

743   Von König, M., Bremer, H., Kleinböhl, A., Küllmann, H., Künzi, K. F., Goede, A. P. H.,

744   Browell, E. V., Grant, W. B., Burris, J. F., McGee, T. J., and Twigg, L.: Using gas-phase nitric

745   acid as an indicator of PSC composition, J. Geophys. Res., 107, D20, 8265,

746   doi:10.1029/2001JD001041, 2002.

747

748

NH, 11 Jan 1979, 31.6 hPa
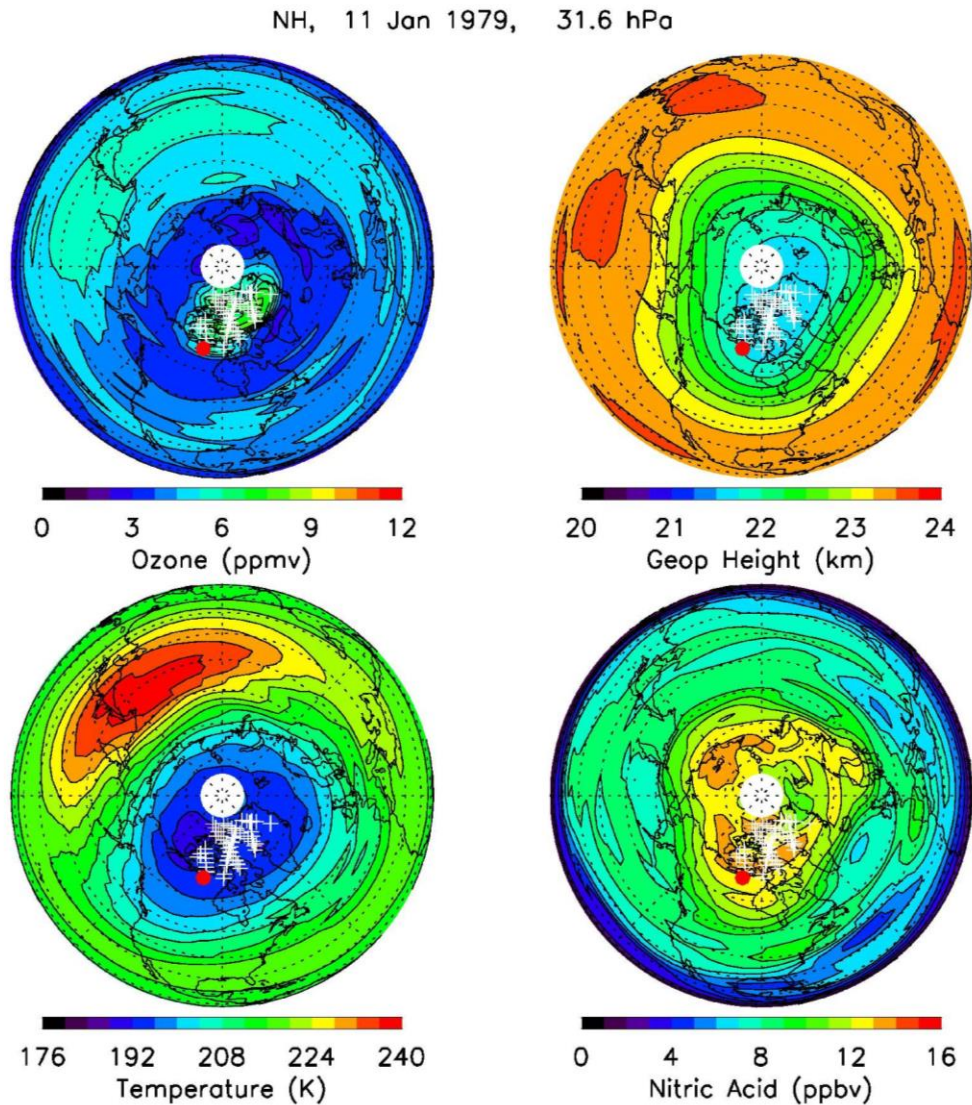
Figure 1. Polar orthographic projections of Northern Hemisphere ozone (top left), geopotential height (GPH, top right), temperature (bottom left), and gas phase nitric acid (bottom right) for 11 January 1979 at 31.6 hPa; successive latitude circles are at every 10˚. The Greenwich meridian extends horizontally to the right. Contour intervals are every 0.75 ppmv for ozone, 0.25 km for GPH, 4 K for temperature, and 1 ppbv for nitric acid. White plus signs denote orbital profile segments that are missing; red dot denotes location of a SAM II PSC observation.

NH, 17 Jan 1979, 31.6 hPa

(a)

−2.50 −1.25 0.00 1.25 2.50
Ozone (ppmv)

(b)

−1.50 −0.75 0.00 0.75 1.50
Geop Height (km)

(c)

−3.0 −1.5 0.0 1.5 3.0
Nitrogen Dioxide (ppbv)

(d)

−4 −2 0 2 4
Nitric Acid (ppbv)
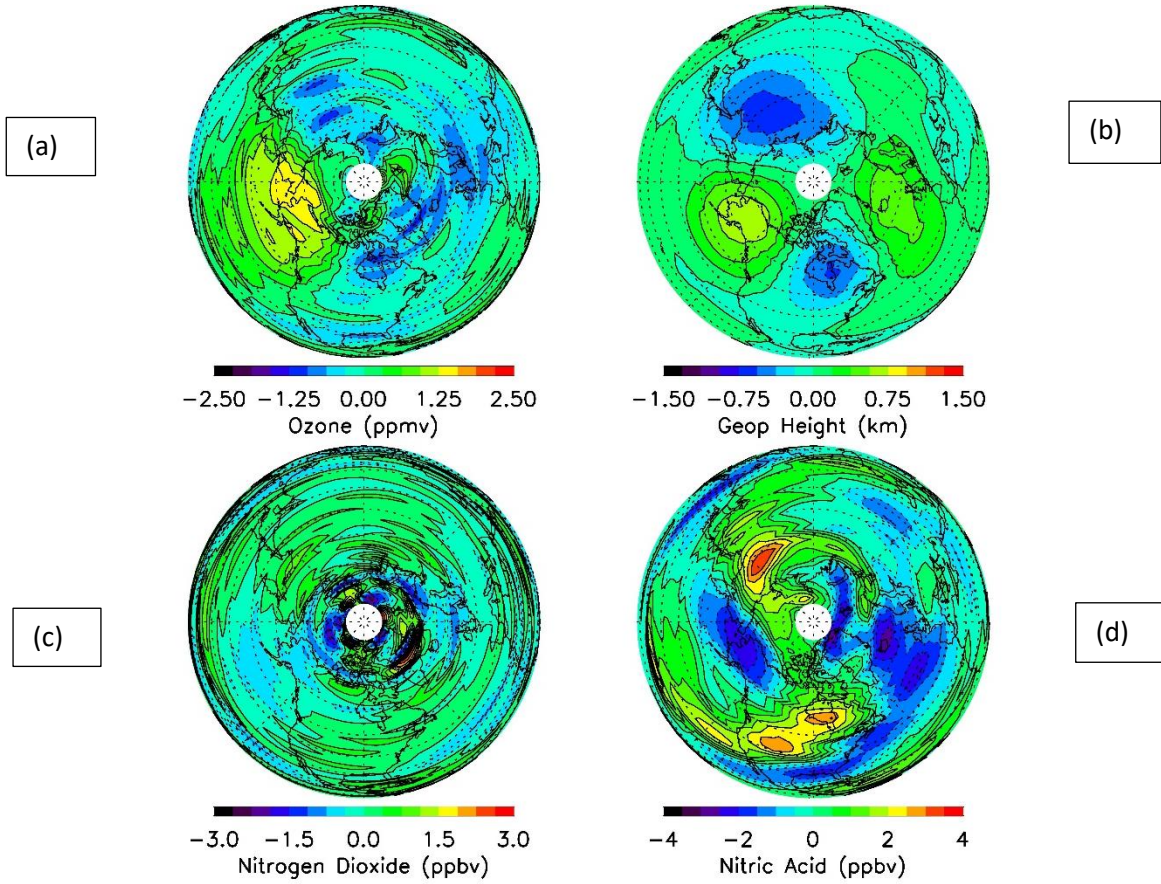
757

758

759 **Figure 2.** Zonal anomalies of ozone, GPH, nitrogen dioxide, and nitric acid for 31.6 hPa on 17

760 January 1979.

761

762

NH, 27 Jan 1979, 31.6 hPa

(a)

−2.50 −1.25 0.00 1.25 2.50
Ozone (ppmv)

(b)

−1.50 −0.75 0.00 0.75 1.50
Geop Height (km)

(c)

−3.0 −1.5 0.0 1.5 3.0
Nitrogen Dioxide (ppbv)

(d)

−4 −2 0 2 4
Nitric Acid (ppbv)

763

764
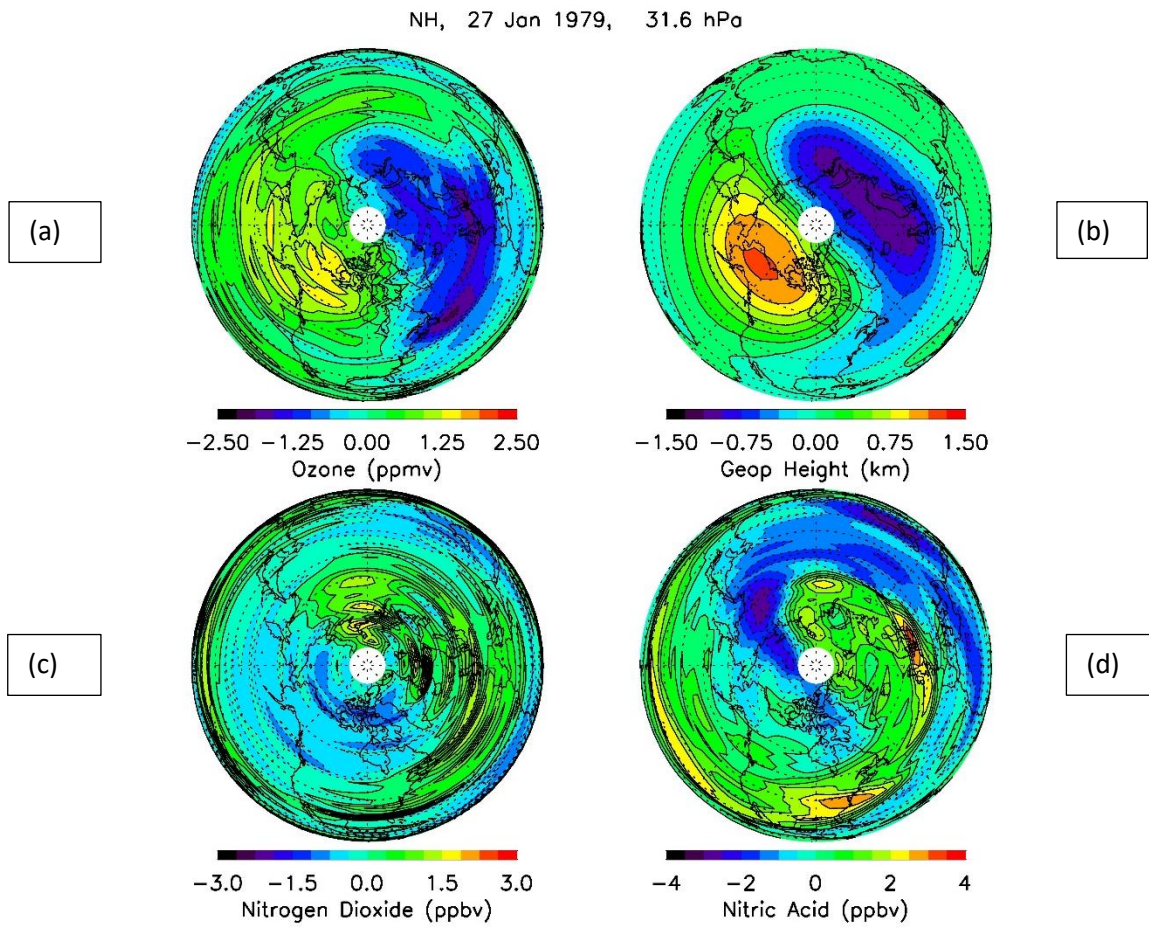
Figure 3. As in Fig. 2, but for 27 January 1979.

766
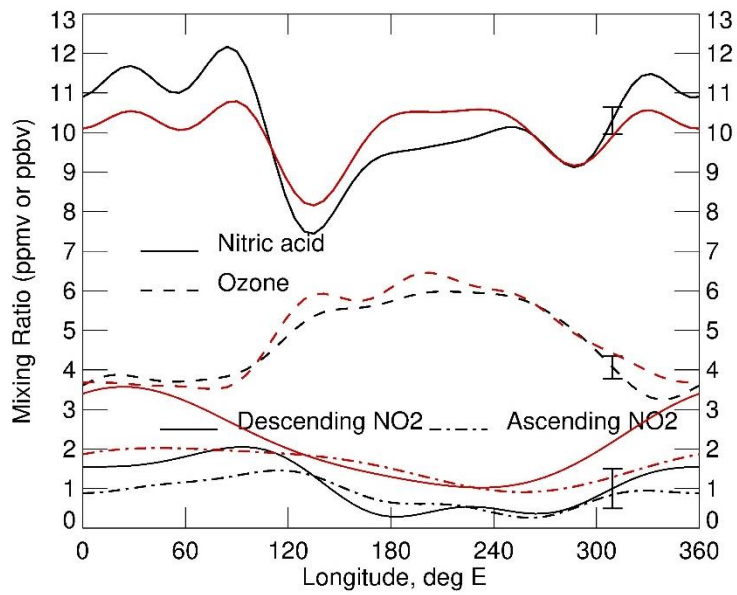
Figure 4. Zonal variations of LIMS V6 (black) and V5 (red) species at 64˚ N on 27 January
1979. Vortex is between 0 and 90° E, and AH region is from 180 and 240° E. Vertical bars on
curves near 311°E are 2σ estimates of the error. Ozone has units of ppmv, while HNO_3 and NO_2
(its separate descending and ascending curves at bottom) have units of ppbv.
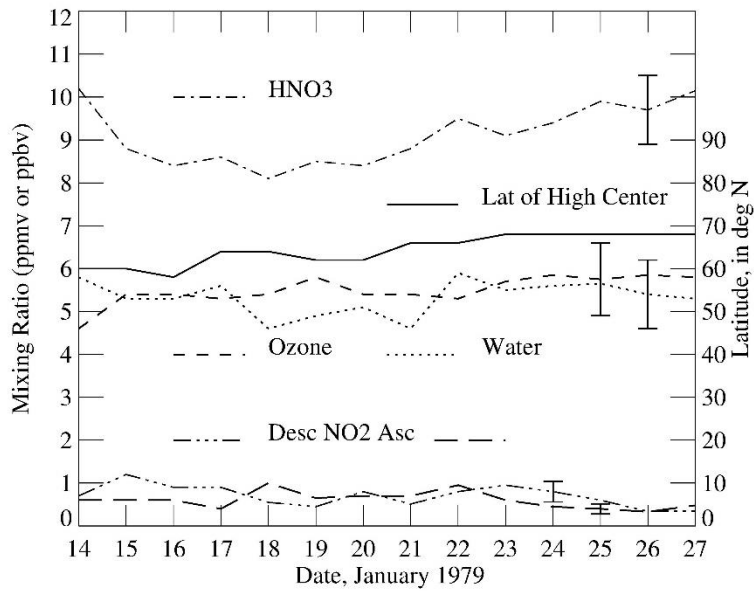
Figure 5. Time series of observed LIMS V6 species at 31.6 hPa and the Aleutian High (AH) anomaly; latitude of AH center is the solid curve. The species curves have vertical bars near 24 to 26 January indicating their ±RSS errors. Ozone and water have units of ppmv, while NO_2 and HNO_3 have units of ppbv.

782

783
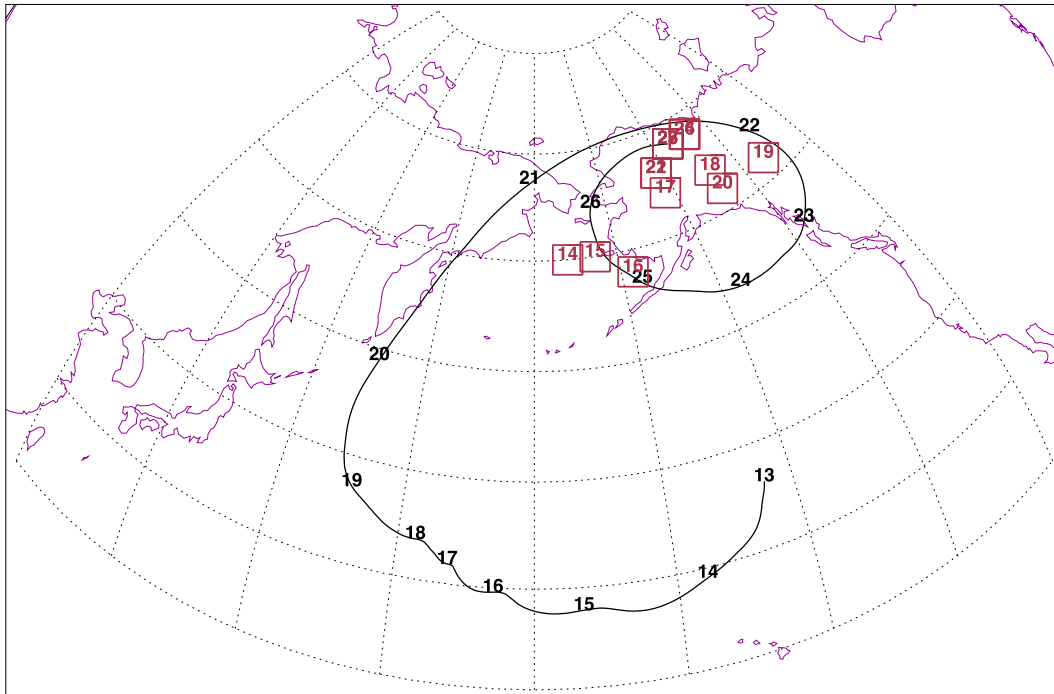
Figure 6. History of the location of maximum GPH anomaly at 31.6 hPa representing the AH center and displayed by red squares with day numbers. Latitude spacing is 10° beginning at 20° N and longitude spacing is 15° beginning at 120° E. Note that between 21 and 27 January there is some repetition of the AH center locations, and the corresponding red squares overlap. The location on 27 January is 214° E and 68°N. Black line with day numbers describes the back trajectory beginning at 214° E, 68° N, and 30 hPa.

790

(a)

(b)
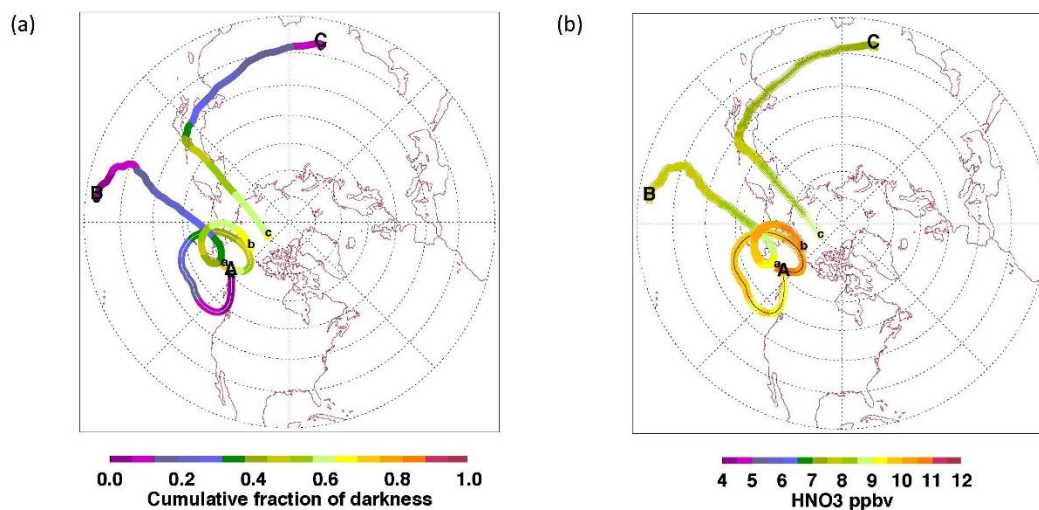
794   **Figure 7.** (a) Back trajectories beginning at 11 pm on 27 January (9Z on January 28) from 30

795   hPa, 214° E, and three different latitudes **[a]** 60° N, **[b]** 72° N, and **[c]** 80° N. The corresponding

796   endpoints **A, B**, and **C** are spatially and temporally closest to LIMS descending mode

797   measurement locations between 14 and 17 January. The latitude grids are 10° apart, starting

798   from 20° N and the Prime meridian extends horizontally to the right. The color scale refers to

799   the accumulated hours of darkness expressed as a fraction of the total length of the trajectory in

800   hours as the air parcel moves in the forward direction starting from locations **A, B,** and **C** and

801   ending at **a, b,** or **c** along 214° E longitude. (b) Evolution of HNO_3 along the three trajectories

802   that were shown in (a).

803

804
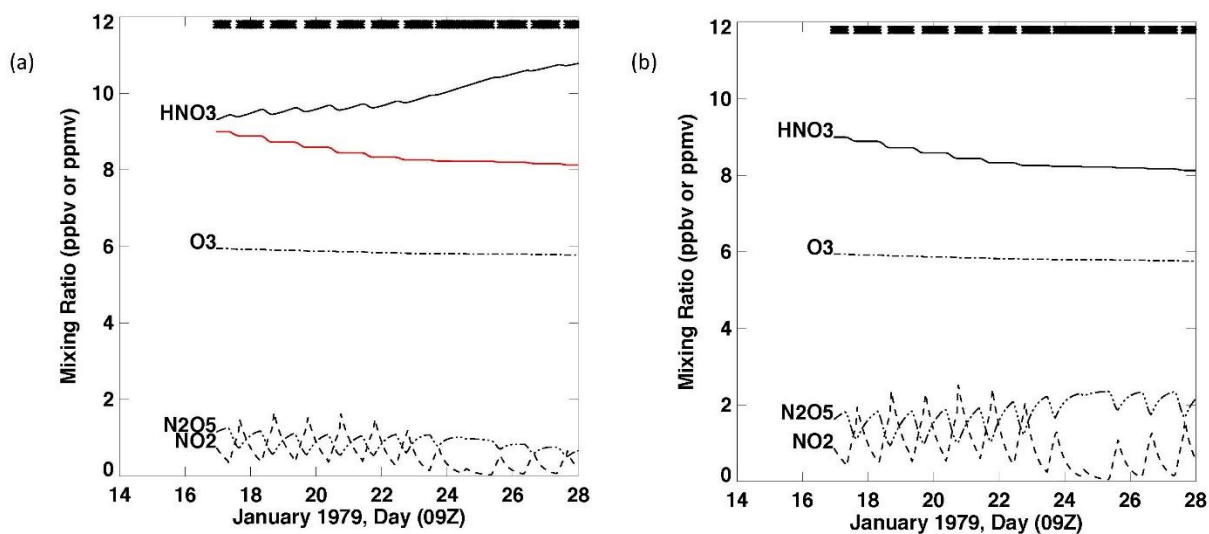
805

806

807 **Figure 8.** Mixing ratio of selected species as a function of time along the trajectory A-a shown

808 in Figure 7a. Air parcel terminates at $214°$ E and $60°$ N. HNO_3 (solid), NO_2 (dash), and N_2O_5

809 (dash-dot-dot) are in ppbv, and ozone (dash-dot) is in ppmv. The tick marks on the abscissa

810 correspond to 09Z hours on the dates shown. The thick line at the top represents the periods of

811 darkness along the trajectory with intermittent gaps corresponding to sunlit segments. (a)

812 Results from the case including heterogeneous reactions, but with the red curve showing HNO_3

813 from only the gas phase chemistry for comparison; (b) Results for all species from only the gas

814 phase reactions.

815

816

817

818
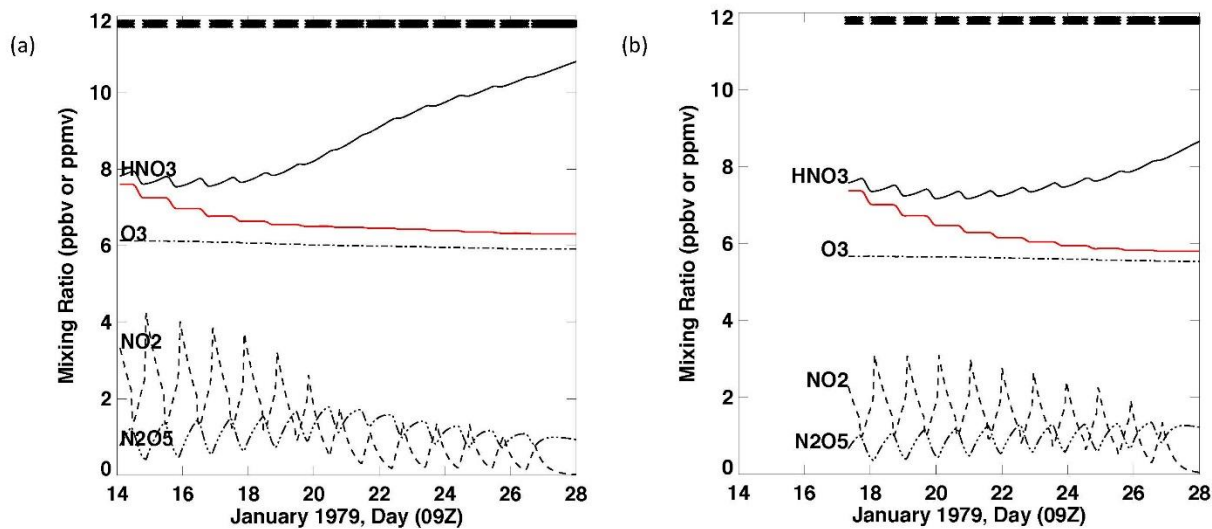
Figure 9. Mixing ratio of selected species as a function of time for the case with heterogeneous
reactions as shown in Figure 8a but for trajectory B-b (a) and trajectory C-c (b). HNO_3 (solid),
NO_2 (dash), and N_2O_5 (dash-dot-dot) are in ppbv, and ozone (dash-dot) is in ppmv. The red
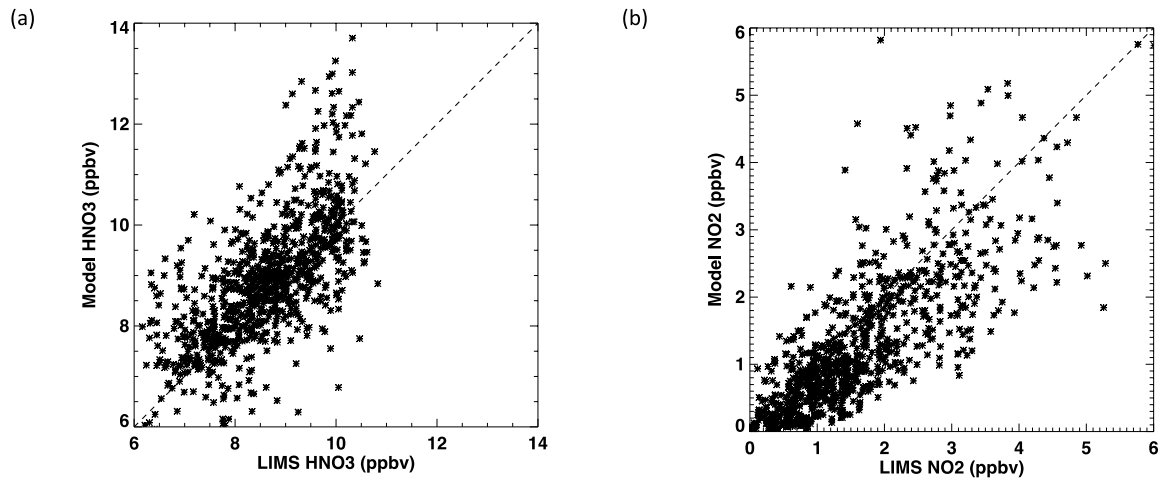curve in both panels represent the HNO_3 variation for the case with only gas phase reactions.

823

824
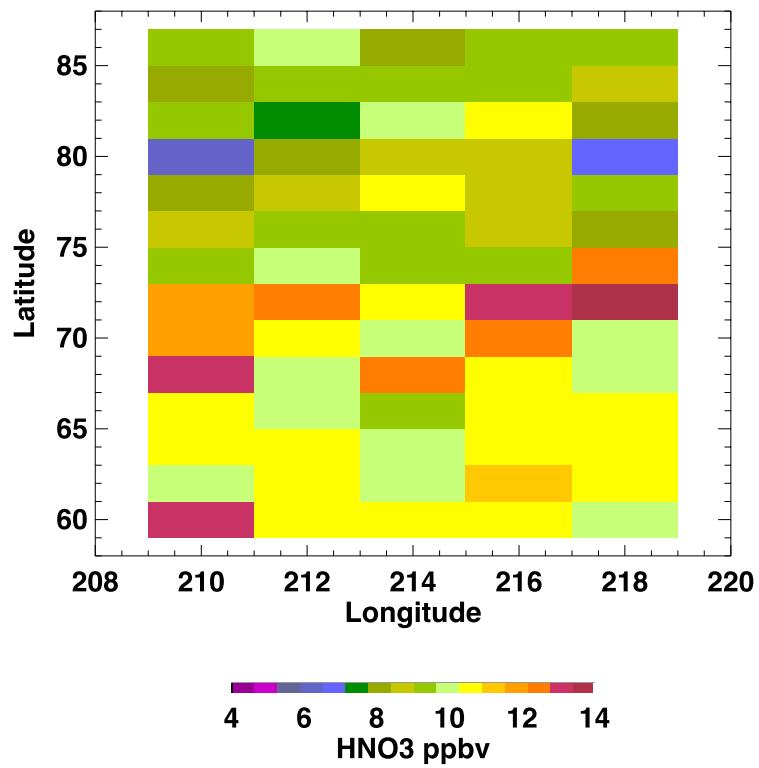
Figure 10. Calculated HNO₃ at 09Z on 28 January, corresponding to terminal location of all 70 trajectories.

825

826

827

828

829

(a)

(b)

Figure 11. Scatter plot of calculated species mixing ratios along the 70 trajectories and of the corresponding spatially and temporally closest LIMS V6 observation. (a) HNO_3; (b) NO_2.
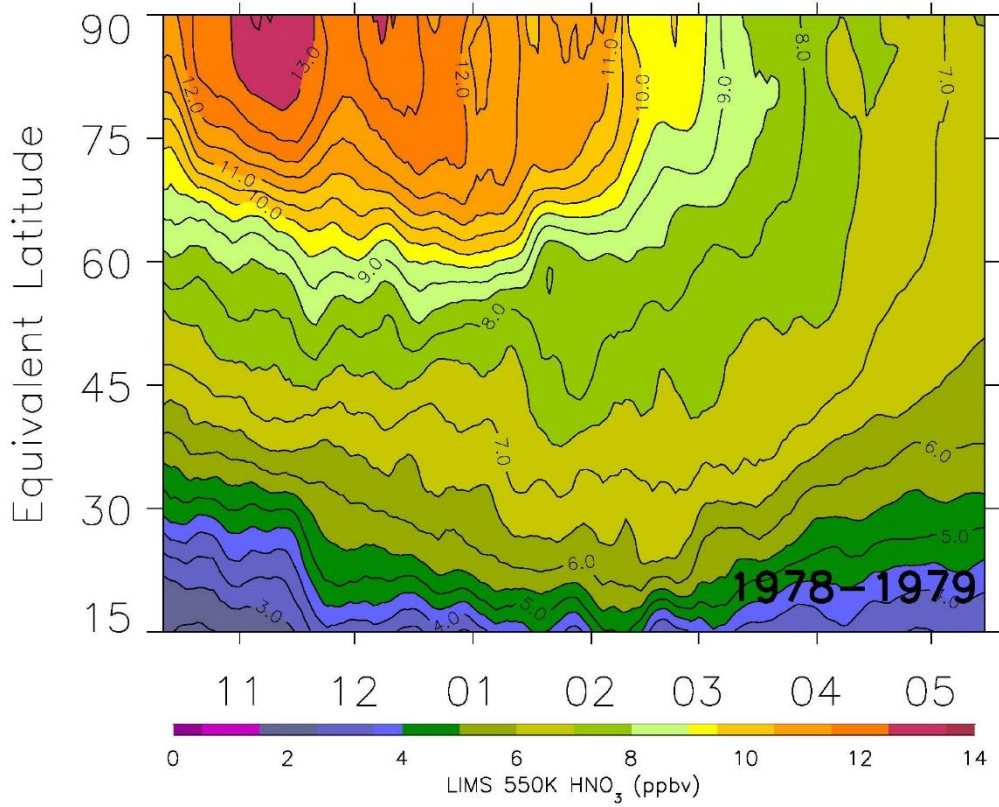
835
836
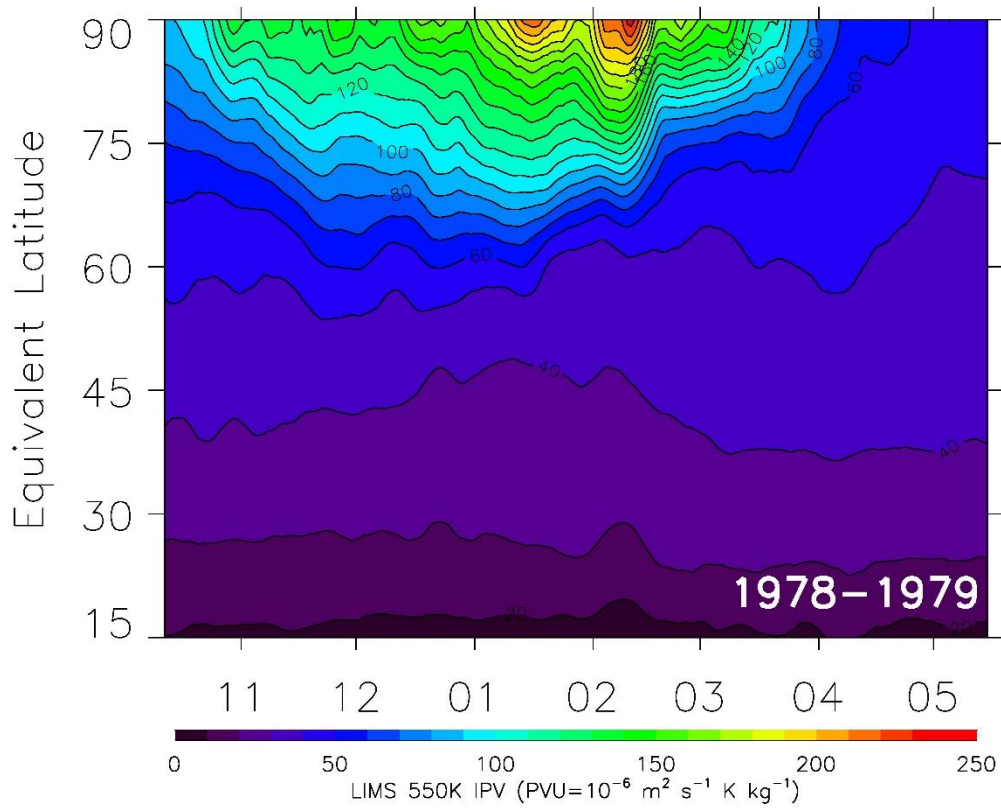
Figure 12. Time series of LIMS isentropic PV versus equivalent latitude at 550 K and with smoothing over 7 days. PV contour interval (CI) is 10 units.

842

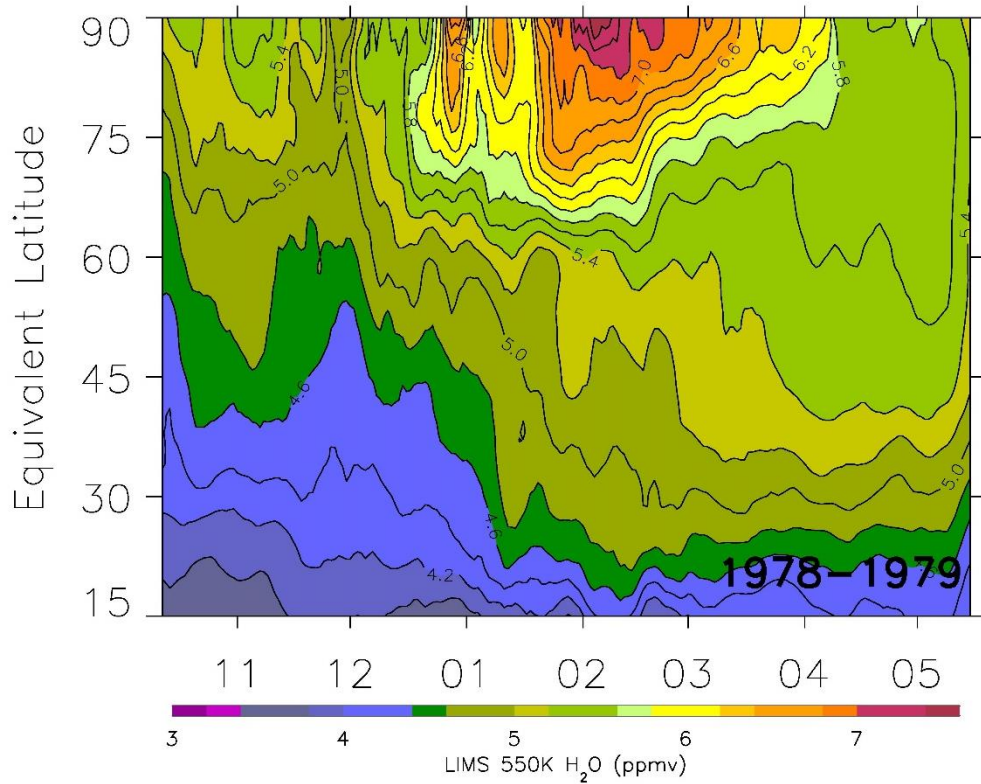**Figure 13.** As in Fig. 12, but the averages of HNO_3 along PV isolines (CI is 0.5 ppbv).
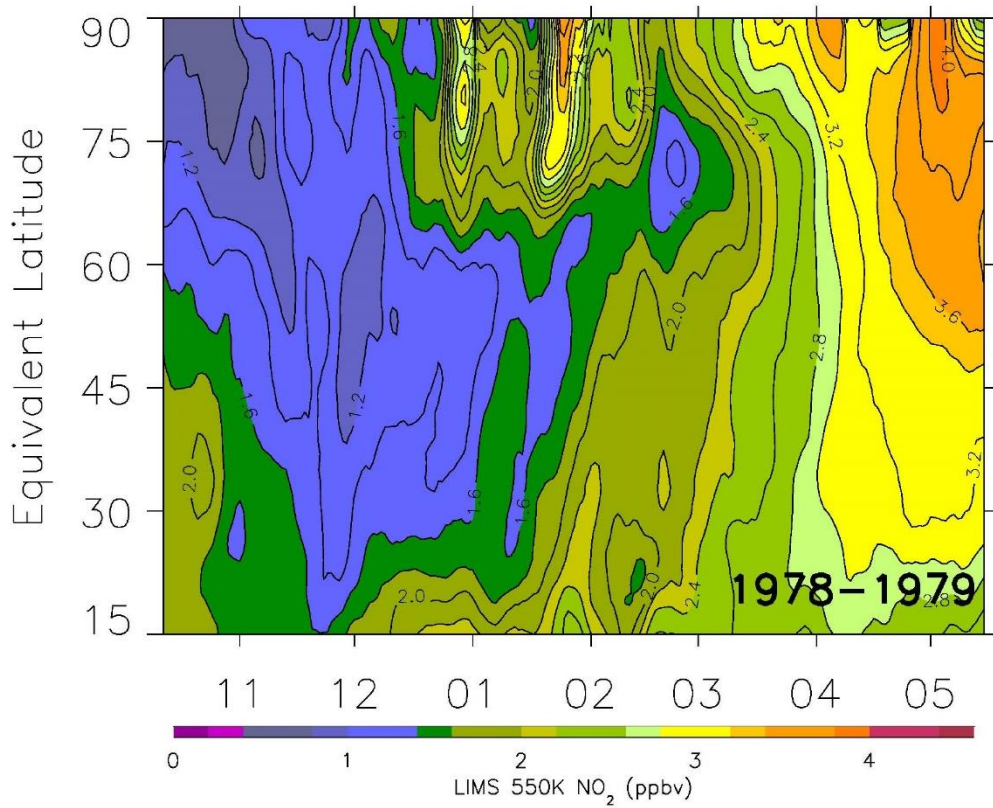
844

845

846

847 **Figure 14**. As in Fig. 13, but as averages of H_2O (CI = 0.2 ppmv).

848

849

850

Figure 15. As in Fig. 13, but as averages of descending orbital (nighttime) NO_2 (CI = 0.2 ppbv).

852